ELSEVIER

J. Non-Newtonian Fluid Mech. 142 (2007) 135–142

Journal of Non-Newtonian Fluid Mechanics

www.elsevier.com/locate/jnnfm

# Cessation of annular Poiseuille flows of Bingham plastics

Maria Chatzimina [a], Christos Xenophontos [a], Georgios C. Georgiou [a,*], Ioannis Argyropaidas [b], Evan Mitsoulis [b]

[a] *Department of Mathematics and Statistics, University of Cyprus, P.O. Box 20537, 1678 Nicosia, Cyprus*

[b] *School of Mining Engineering and Metallurgy, National Technical University of Athens, Heroon Polytechniou 9, 157 80 Zografou, Athens, Greece*

Received 29 January 2006; received in revised form 22 May 2006; accepted 4 July 2006

**Abstract**

We numerically solve the cessation of the annular Poiseuille flow of Bingham plastics for various values of the diameter ratio, using the regularized constitutive equation proposed by Papanastasiou and employing finite elements in space and a fully implicit scheme in time. When the yield stress is not zero, the calculated stopping times are finite and just below the theoretical upper bounds provided by Glowinski [R. Glowinski, Numerical Methods for Nonlinear Variational Problems, Springer-Verlag, New York, 1984].


*Keywords:* Annular Poiseuille flow; Bingham plastic; Papanastasiou model; Cessation

## 1. Introduction

Viscoplastic flows have generated a strong scientific interest, as evidenced at the recent workshop on viscoplasticity, that took place in Banff, Canada [1]. Many engineering fields were represented from the flow of avalanches to those of gels. In particular, a drilling equipment in the petroleum industry often operates with viscoplastic fluids, such as drilling muds exhibiting a yield stress [2]. The geometry where the flow takes place is that of an annulus, and therefore a considerable practical interest is generated for these types of annular flows of viscoplastic fluids. The ability to understand and predict these flows in start-up and cessation are of immediate interest to the practitioners in the field.

In a recent work [3], we solved numerically the cessation of the plane Couette and plane and axisymmetric Poiseuille flows of Bingham plastics using the regularized constitutive equation proposed by Papanastasiou [4], in order to avoid the determination of the yielded and unyielded regions in the flow domain. An excellent review by Frigaard and Nouar [5] on different models and their implementation has also recently appeared. It has been generally accepted that for engineering calculations the Papanastasiou model offers an attractive alternative to the ideal Bingham model [4]. Thus, our previous numerical results showed that the numerical stopping times are just below the theoretical upper bounds derived by Glowinski [6] and Huilgol et al. [7]. The objectives of the present work are: (a) to numerically solve, for the first time, the cessation of the annular Poiseuille flow of a Bingham fluid for different diameter ratios, using a regularized model and (b) to compute the stopping times and make comparisons with the theoretical upper bound given by Glowinski [6].

The paper is organized as follows. In Section 2, we present the steady-state and time-dependent solutions for the Newtonian annular Poiseuille flow. In Section 3, we present the steady-state solution for the annular Poiseuille flow of a Bingham plastic and the theoretical upper bounds for the stopping times in the case of flow cessation. In Section 4, we introduce the regularized Papanastasiou constitutive equation, discuss briefly the numerical method, and present results for various diameter ratios. Comparisons are also made with the theoretical stopping time bounds, which indicate that the latter are tight. Some discrepancies are observed only for low Bingham numbers when the growth parameter in the Papanastasiou model is not sufficiently high. Finally, Section 5 contains the conclusions of this work.

## 2. Newtonian annular Poiseuille flow

We consider the Poiseuille flow of a Newtonian fluid in an annulus of radii $\kappa R$ and $R$, where $0 < \kappa < 1$, as shown in Fig. 1.

* Corresponding author. Tel.: +357 22892612; fax: +357 22892601.
*E-mail address:* georgios@ucy.ac.cy (G.C. Georgiou).

0377-0257/$ – see front matter © 2006 Elsevier B.V. All rights reserved.
doi:10.1016/j.jnnfm.2006.07.002

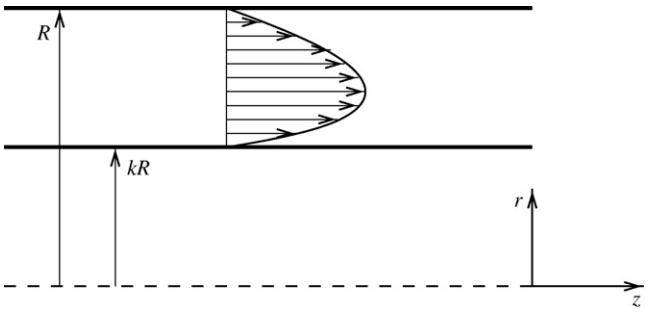


Fig. 1. Geometry of the annular Poiseuille flow of a Newtonian fluid.

### 2.1. Steady-state Newtonian flow

The steady-state velocity profile is given by [8]

$$u_z^{\mathrm{s}}(r) = \frac{1}{4\mu}\left(-\frac{\partial p}{\partial z}\right)^{\mathrm{s}}\left[1-\left(\frac{r}{R}\right)^2+\frac{1-\kappa^2}{\ln(1/\kappa)}\ln\frac{r}{R}\right], \tag{1}$$

where $(-\partial p/\partial z)^{\mathrm{s}}$ is the (steady-state) pressure gradient and $\mu$ is the constant viscosity. The volumetric flow rate, $Q$, and the mean velocity in the annulus, $V$, are given by

$$Q = \frac{\pi}{8\mu}\left(-\frac{\partial p}{\partial z}\right)^{\mathrm{s}} R^4\left[1-\kappa^4-\frac{(1-\kappa^2)^2}{\ln(1/\kappa)}\right] \tag{2}$$

and

$$V = \frac{1}{8\mu}\left(-\frac{\partial p}{\partial z}\right)^{\mathrm{s}} R^2\left[1+\kappa^2-\frac{1-\kappa^2}{\ln(1/\kappa)}\right]. \tag{3}$$

To nondimensionalize the equations, we scale lengths by $R$, the velocity by $V$, and the pressure and stress components by $\mu V/R$. The dimensionless axial velocity is then given by

$$(u_z^{\mathrm{s}})^*(r^*) = \frac{2}{1+\kappa^2-((1-\kappa^2)/\ln(1/\kappa))} \times\left[1-(r^*)^2+\frac{1-\kappa^2}{\ln(1/\kappa)}\ln r^*\right]. \tag{4}$$

For simplicity, the stars (*) are dropped hereafter.

In Fig. 2, we plot the dimensionless steady-state Newtonian velocity profiles for various values of $\kappa$. The maximum of the velocity occurs at

$$r_{\mathrm{m}} = \left[\frac{1-\kappa^2}{2\ln(1/\kappa)}\right]^{1/2}. \tag{5}$$

The dimensionless pressure gradient, denoted by $f^{\mathrm{s}}$, is given by

$$f^{\mathrm{s}} = \frac{8}{1+\kappa^2-((1-\kappa^2)/\ln(1/\kappa))}. \tag{6}$$

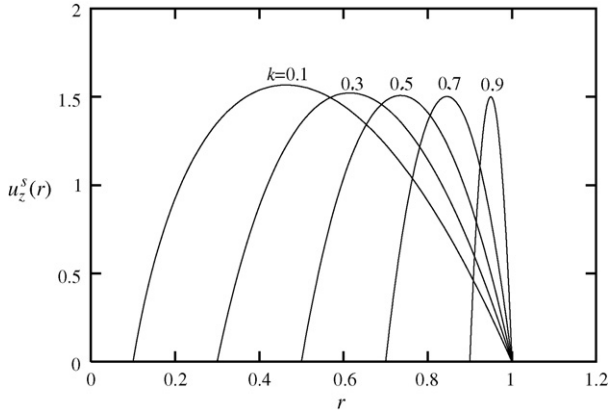


Fig. 2. Steady Newtonian velocity profiles for different values of $\kappa$.

### 2.2. Cessation of the Newtonian flow

We assume that at $t=0$ the velocity $u_z(r, t)$ is given by the steady-state solution (Eq. (1)) and that at $t=0^+$ the pressure gradient is changed from $(-\partial p/\partial z)^{\mathrm{s}}$ to $(-\partial p/\partial z)$. Scaling the time by $\rho R^2/\mu$, we obtain the dimensionless form of the $z$-momentum equation:

$$\frac{\partial u_z}{\partial t} = f+\frac{1}{r}\frac{\partial}{\partial r}\left(r\frac{\partial u_z}{\partial r}\right), \tag{7}$$

where $f$ is the new pressure gradient. The dimensionless boundary and initial conditions read:

$$\left.\begin{aligned} &u_z(\kappa, t) = 0, \quad t\geq 0\\ &u_z(1, t) = 0, \quad t\geq 0\\ &u_z(r, 0) = u_z^{\mathrm{s}}(r), \quad \kappa\leq r\leq 1\end{aligned}\right\}. \tag{8}$$

Let $(a_k, b_k)$, $k=1, 2, \ldots$ be the solutions of the system

$$\left.\begin{aligned} &J_0(a_k\kappa)+b_kY_0(a_k\kappa) = 0\\ &J_0(a_k)+b_kY_0(a_k) = 0\end{aligned}\right\}, \tag{9}$$

where $J_0$ and $Y_0$ are, respectively, the zeroth-order Bessel functions of the first and second kind. Let now

$$Z_0^k(r) \equiv J_0(r)+b_kY_0(r) \tag{10}$$

and

$$Z_1^k(r) \equiv J_1(r)+b_kY_1(r), \tag{11}$$

where $J_1$ and $Y_1$ are, respectively, the first-order Bessel functions of the first and second kind. Then the system (9) takes the simpler form:

$$\left.\begin{aligned} &Z_0^k(a_k\kappa) = 0\\ &Z_0^k(a_k) = 0\end{aligned}\right\}. \tag{12}$$

It can be shown that the time-dependent solution, when the pressure gradient is suddenly reduced from $f^{\mathrm{s}}\neq 0$ to $f$, is given by [9]

$$u_z(r, t) = a'\frac{f}{f^{\mathrm{s}}}\left[1-r^2+\frac{1-\kappa^2}{\ln(1/\kappa)}\ln r\right] +8a'\left(1-\frac{f}{f^{\mathrm{s}}}\right)\sum_{k=1}^{\infty}\frac{1}{a_k^3}\frac{Z_0^k(a_kr)}{Z_1^k(a_k)+\kappa Z_1^k(a_k\kappa)}\mathrm{e}^{-a_k^2t}, \tag{13}$$

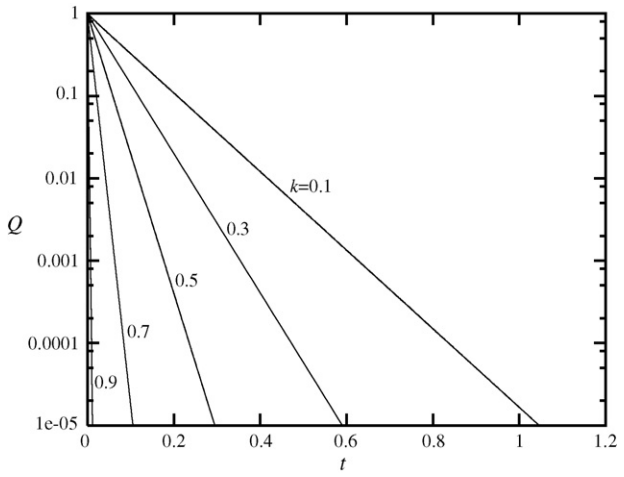


Fig. 3. Evolution of the volumetric flow rate in cessation of annular Newtonian Poiseuille flow for various values of $\kappa$.

where

$$a' = \frac{2}{1+\kappa^2 - ((1-\kappa^2)/\ln(1/\kappa))}. \tag{14}$$

Integrating Eq. (13) gives the dimensionless volumetric flow rate which is scaled by $\pi(1-\kappa^2)$:

$$Q = \frac{32}{1-\kappa^4 - ((1-\kappa^2)^2/\ln(1/\kappa))} \times \sum_{k=1}^{\infty} \frac{1}{a_k^4} \frac{Z_1^k(a_k) - \kappa Z_1^k(a_k\kappa)}{Z_1^k(a_k) + \kappa Z_1^k(a_k\kappa)} e^{-a_k^2 t}. \tag{15}$$

The volumetric flow rate decays exponentially with time (i.e. the stopping time is infinite). In Fig. 3, we see the predictions of Eq. (15) for various values of $\kappa$.

## 3. Annular Poiseuille flow of a Bingham fluid

Let $\mathbf{u}$, $\boldsymbol{\tau}$, and $\dot{\boldsymbol{\gamma}}$ denote, respectively, the velocity vector, the stress tensor, and the rate-of-strain tensor. The latter is defined by:

$$\dot{\boldsymbol{\gamma}} \equiv \nabla\mathbf{u} + (\nabla\mathbf{u})^{\mathrm{T}}, \tag{16}$$

where $\nabla\mathbf{u}$ is the velocity-gradient tensor, and the superscript 'T' denotes its transpose. The magnitudes of $\dot{\boldsymbol{\gamma}}$ and $\boldsymbol{\tau}$ are, respectively, defined as follows:

$$\dot{\gamma} = \sqrt{\frac{1}{2}\mathrm{II}_{\dot{\boldsymbol{\gamma}}}} = \sqrt{\frac{1}{2}\dot{\boldsymbol{\gamma}} : \dot{\boldsymbol{\gamma}}} \quad \text{and} \quad \tau = \sqrt{\frac{1}{2}\mathrm{II}_{\boldsymbol{\tau}}} = \sqrt{\frac{1}{2}\boldsymbol{\tau} : \boldsymbol{\tau}}, \tag{17}$$

where II stands for the second invariant of a tensor. In tensorial form, the Bingham model is written as follows:

$$\begin{cases} \dot{\boldsymbol{\gamma}} = \mathbf{0}, & \tau \le \tau_0 \\ \boldsymbol{\tau} = \left(\dfrac{\tau_0}{\dot{\gamma}} + \mu\right)\dot{\boldsymbol{\gamma}}, & \tau \ge \tau_0 \end{cases} \tag{18}$$

where $\tau_0$ is the yield stress.

### 3.1. Steady-state Bingham flow

The steady-state annular Poiseuille flow of a Bingham fluid has been solved by Bird et al. [10]. Szabo and Hassager [11] have also presented analytical solutions for the flow of a Bingham fluid in general eccentric annular geometries.

For any fluid, the steady-state one-dimensional $z$-momentum equation is

$$0 = \left(-\frac{\partial p}{\partial z}\right)^{\mathrm{s}} + \frac{1}{r}\frac{\mathrm{d}}{\mathrm{d}r}(r\tau_{rz}), \tag{19}$$

which upon integration yields

$$\tau_{rz} = -\left(-\frac{\partial p}{\partial z}\right)^{\mathrm{s}} \frac{r}{2} + \frac{c}{r}, \tag{20}$$

where $c$ is the integration constant. In the case of a pressure-driven Bingham flow in an annulus, the flow field is divided into three flow regions as shown in Fig. 4, where we use the notation of Bird et al. [10]. In region I ($\kappa R \le r \le \lambda_- R$), $\tau_{rz} \ge \tau_0$ with

$$\dot{\gamma} = \frac{\mathrm{d}u_z}{\mathrm{d}r} \quad \text{and} \quad \tau_{rz} = \tau_0 + \mu\frac{\mathrm{d}u_z}{\mathrm{d}r}. \tag{21}$$

In region II ($\lambda_+ R \le r \le R$), $-\tau_{rz} \ge \tau_0$ with

$$\dot{\gamma} = -\frac{\mathrm{d}u_z}{\mathrm{d}r} \quad \text{and} \quad \tau_{rz} = -\tau_0 + \mu\frac{\mathrm{d}u_z}{\mathrm{d}r}. \tag{22}$$

Finally, in region III ($\lambda_- R \le r \le \lambda_+ R$), $|\tau_{rz}| \le \tau_0$ and

$$\dot{\gamma} = \frac{\mathrm{d}u_z}{\mathrm{d}r} = 0, \tag{23}$$

which means that the fluid is unyielded.

By requiring that

$$\tau_{rz}(\lambda_- R) = -\tau_{rz}(\lambda_+ R) = \tau_0, \tag{24}$$

one finds that

$$2\tau_0 = (\lambda_+ - \lambda_-)R\left(-\frac{\partial p}{\partial z}\right)^{\mathrm{s}} \tag{25}$$

and

$$c = \frac{\lambda_-\lambda_+}{2}R^2\left(-\frac{\partial p}{\partial z}\right)^{\mathrm{s}} = \frac{\lambda_-\lambda_+}{\lambda_+ - \lambda_-}\tau_0 R. \tag{26}$$

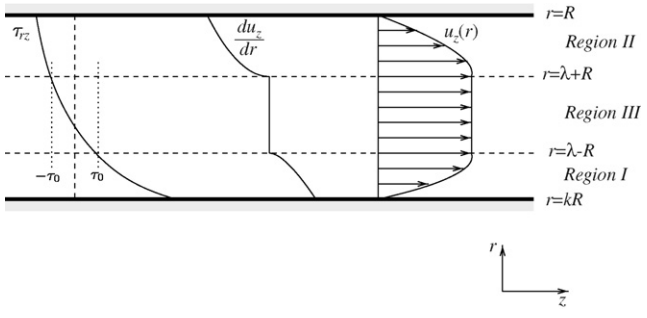


Fig. 4. Profiles of the shear stress, the shear rate and the velocity in the annular Poiseuille flow of a Bingham fluid.

Substituting Eq. (26) into Eq. (20) gives

$$\tau_{rz} = -\frac{R}{2}\left(-\frac{\partial p}{\partial z}\right)^{s}\left[\frac{r}{R} - \lambda_-\lambda_+\frac{R}{r}\right]. \tag{27}$$

Substituting now Eq. (21) into Eq. (27), integrating and applying the boundary condition $u_z(\kappa R) = 0$ gives the velocity profile in region I. Similarly, substituting Eq. (22) into Eq. (27), integrating and applying the boundary condition $u_z(R) = 0$ gives the velocity profile in region II. In region III, the velocity is uniform, e.g.

$$u_z(r) = u_z(\lambda_+ R), \quad \lambda_- R \le r \le \lambda_+ R. \tag{28}$$

The following velocity profile is thus obtained:

$$u_z(r) = \frac{1}{4\mu}R^2\left(-\frac{\partial p}{\partial z}\right)^{s}\begin{cases}\left[2\lambda_-\lambda_+ \ln\frac{r}{\kappa R} - \frac{r^2}{R^2} + \kappa^2 - 2(\lambda_+ - \lambda_-)\left(\frac{r}{R} - \kappa\right)\right], & \kappa R \le r \le \lambda_- R\\ \left[-2\lambda_-\lambda_+ \ln\frac{1}{\lambda_+} + 1 - \lambda_+^2 - 2(\lambda_+ - \lambda_-)(1 - \lambda_+)\right], & \lambda_- R \le r \le \lambda_+ R\\ \left[-2\lambda_-\lambda_+ ln\frac{R}{r} + 1 - \frac{r^2}{R^2} - 2(\lambda_+ - \lambda_-)\left(1 - \frac{r}{R}\right)\right], & \lambda_+ R \le r \le R\end{cases} \tag{29}$$

By demanding that

$$u_z(\lambda_- R) = u_z(\lambda_+ R), \tag{30}$$

we find an equation relating $\lambda_+$ to $\lambda_-$ and $\kappa$:

$$\left(2\beta \ln\frac{\beta}{\kappa} + \beta^2 - 1\right)\lambda_+^2 + 2(1-\beta)(1+\kappa)\lambda_+ - 1 + \kappa^2 = 0, \tag{31}$$

where

$$\beta = \frac{\lambda_-}{\lambda_+}. \tag{32}$$

For given $\kappa$ and $\beta$, $\lambda_+$ is the root of the quadratic Eq. (31) between $\lambda_-$ and 1.

We now note from Eq. (25) that when $\tau_0 = 0$, then $\lambda_- = \lambda_+$, which corresponds to the Newtonian flow (the unyielded region degenerates to the velocity maximum). Moreover, the critical pressure above which Bingham flow occurs corresponds to $\lambda_- = \kappa$ and $\lambda_+ = 1$, i.e. the entire flow field is an unyielded region. It is clear that flow occurs only when

$$\left(-\frac{\partial p}{\partial z}\right)^{s} > \frac{2\tau_0}{(1-\kappa)R}. \tag{33}$$

In Fig. 5, we plot $\lambda_-$ and $\lambda_+$, calculated from Eq. (31) for $\kappa = 0.1$ and 0.5, versus the dimensionless number

$$\chi \equiv \frac{\lambda_+ - \lambda_-}{1-\kappa} = \frac{2\tau_0}{(1-\kappa)R(-\partial p/\partial z)^{s}}. \tag{34}$$

For $\chi = 0$, the two yield points coincide with the maximum of the Newtonian velocity given by Eq. (5). When $\chi = 1$ the pressure gradient is equal to the critical one and no flow occurs.

Integrating the velocity profile (29) over the annular cross section gives the following expression for the volumetric flow rate:

$$Q = \frac{\pi}{8\mu}\left(-\frac{\partial p}{\partial z}\right)^{s}R^4\left[1 - \kappa^4 - 2\beta\lambda_+^2(1-\kappa^2) - \frac{4}{3}(1-\beta)\lambda_+(1+\kappa^3) + \frac{1}{3}\lambda_+^4(1-\beta^2)(1+\beta)^2\right]. \tag{35}$$

For the mean velocity in the annulus, we get

$$V = \frac{1}{8\mu}\left(-\frac{\partial p}{\partial z}\right)^{s}R^2\frac{I}{1-\kappa^2}, \tag{36}$$

where

$$I = \left[1 - \kappa^4 - 2\beta\lambda_+^2(1-\kappa^2) - \frac{4}{3}(1-\beta)\lambda_+(1+\kappa^3) + \frac{1}{3}\lambda_+^4(1-\beta^2)(1+\beta)^2\right]. \tag{37}$$

We nondimensionalize the equations as in the Newtonian flow, i.e. we scale lengths by $R$, the velocity by $V$ and the pressure (and stress components) by $\mu V/R$. For the dimensionless velocity, we get:

$$u_z(r) = \frac{2(1-\kappa^2)}{I}\begin{cases}\left[2\lambda_-\lambda_+ \ln\frac{r}{\kappa} - r^2 + \kappa^2 - 2(\lambda_+ - \lambda_-)(r - \kappa)\right], & \kappa \le r \le \lambda_-\\ \left[-2\lambda_-\lambda_+ \ln\frac{1}{\lambda_+} + 1 - \lambda_+^2 - 2(\lambda_+ - \lambda_-)(1 - \lambda_+)\right], & \lambda_- \le r \le \lambda_+\\ \left[-2\lambda_-\lambda_+ \ln\frac{1}{r} + 1 - r^2 - 2(\lambda_+ - \lambda_-)(1 - r)\right], & \lambda_+ \le r \le 1\end{cases} \tag{38}$$

From Eq. (36), we find the dimensionless pressure gradient:

$$f^{s} = \frac{8(1-\kappa^2)}{I}. \tag{39}$$

From Eq. (25), we get

$$Bn = \frac{\lambda_+ - \lambda_-}{2}f^{s} = \frac{4(\lambda_+ - \lambda_-)}{I}(1-\kappa^2), \tag{40}$$

where

$$Bn \equiv \frac{\tau_0 R}{\mu V} \tag{41}$$

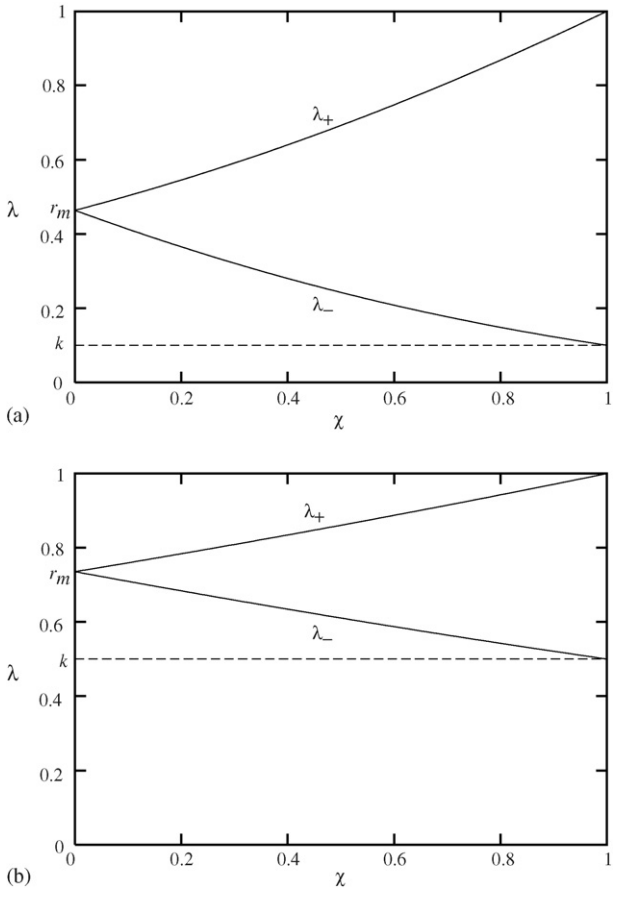


Fig. 5. Evolution of the positions of the two yield points ($\lambda_-$ and $\lambda_+$) with $\chi$ for $\kappa = 0.1$ (a) and 0.5 (b).

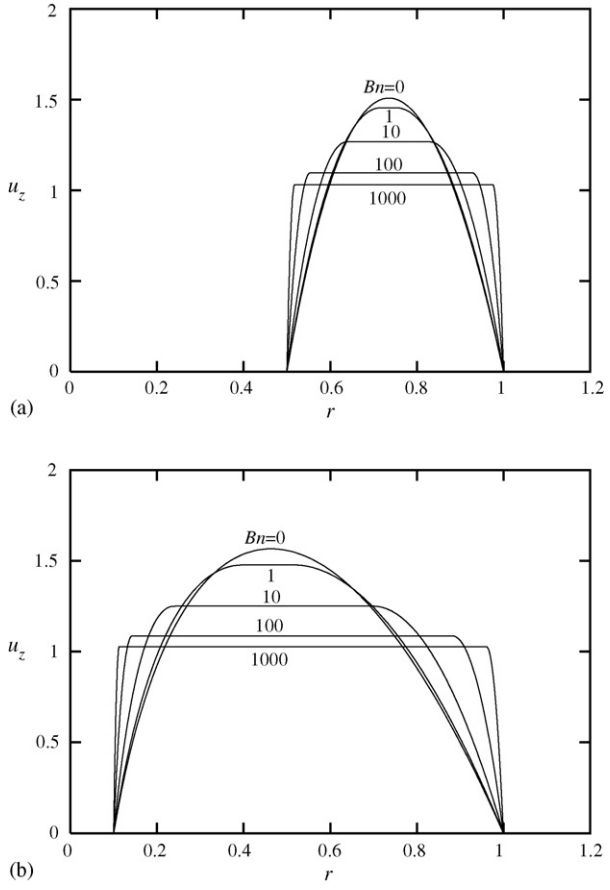


Fig. 6. Dimensionless velocity profiles for different Bingham numbers with (a) $\kappa = 0.5$ and (b) $\kappa = 0.1$.

is the Bingham number. The dimensionless number $\chi$ defined in Eq. (34) takes the form:

$$\chi \equiv \frac{2Bn}{(1-\kappa)f^{\mathrm{s}}}. \tag{42}$$

Obviously, flow occurs only if

$$f^{\mathrm{s}} > \frac{2Bn}{1-\kappa}. \tag{43}$$

In Fig. 6, the dimensionless velocity profiles for $\kappa = 0.5$ and 0.1 are plotted for various Bingham numbers. We observe that the size of the unyielded region increases with the Bingham number and the velocity profile becomes flat as $Bn$ goes to infinity. As the value of $\kappa$ is reduced, the velocity profiles become more asymmetric and skewed towards the inner wall.

### 3.2. Cessation of Bingham flow

We assume that at $t = 0$ the velocity $u_z(r, t)$ is given by the steady-state solution and that at $t = 0^+$ the pressure gradient is reduced either to zero or to $(-\partial p/\partial z) < (-\partial p/\partial z)^{\mathrm{s}}$. Using the same scales as above, we obtain the dimensionless form of the $z$-momentum equation

$$\frac{\partial u_z}{\partial t} = f + \frac{1}{r}\frac{\partial}{\partial r}(r\tau_{rz}), \tag{44}$$

where $f$ is the dimensionless pressure gradient. The dimensionless form of the Bingham constitutive equation is given by

$$\begin{cases} \dot{\gamma} = 0, & |\tau_{rz}| \le Bn \\ \tau_{rz} = \left(\dfrac{Bn}{\dot{\gamma}} + 1\right)\dfrac{\partial u_z}{\partial r}, & |\tau_{rz}| \ge Bn \end{cases} \tag{45}$$

where $\dot{\gamma} = |\partial u_z/\partial r|$. The dimensionless boundary and initial conditions are given by Eq. (8).

Glowinski [6] provides the general expression of the upper bound for the stopping time in the case of a Bingham plastic ($Bn > 0$). For the annular Poiseuille flow, one gets

$$T_f \le \frac{1}{\lambda_1}\ln\left[1 + \lambda_1\frac{||u_z(r,0)||}{(2Bn/(1-\kappa)) - f}\right], \quad f < \frac{2Bn}{1-\kappa}, \tag{46}$$

where $u_z(r, 0) = u_z^{\mathrm{s}}(r)$ is given be Eq. (38),

$$||u_z(r,0)|| = \left[2\int_\kappa^1 u_z^2(r,0)r\,\mathrm{d}r\right]^{1/2}, \tag{47}$$

and $\lambda_1$ is the smallest (positive) eigenvalue of the problem:

$$\frac{1}{r}\frac{\mathrm{d}}{\mathrm{d}r}\left(r\frac{\mathrm{d}w}{\mathrm{d}r}\right) + \lambda w = 0, \quad w(\kappa) = w(1) = 0. \tag{48}$$

Table 1
Least eigenvalues for the upper bound of the stopping time

| $\kappa$ | $a_1$ |
|---|---|
| 0.1 | 3.313938715053 |
| 0.3 | 4.412394692777 |
| 0.5 | 6.246061839191 |
| 0.7 | 10.455235484744 |
| 0.9 | 31.411512705886 |

It is easily found that $\lambda_1 = a_1^2$, where $a_1$ is the smallest eigenvalue of the problem (12), with the corresponding eigenfunction being given by $w_1(x) = Z_0^1(a_1 x)$. Therefore,

$$T_f \leq \frac{1}{a_1^2} \ln\left[1 + a_1^2 \frac{||u_z(r,0)||}{(2Bn/(1-\kappa)) - f}\right], \quad f < \frac{2Bn}{1-\kappa}. \tag{49}$$

Table 1 shows the values of $a_1$ for various values of $\kappa$. These were calculated using the computer algebra system MAPLE [12]. The bound (49) holds only when $f < 2Bn/(1-\kappa)$; otherwise, the flow will not stop.

## 4. Numerical results

As in our previous work [3], in order to simulate the Bingham flow, we employed the regularized constitutive equation proposed by Papanastasiou [4]. In other words, instead of using Eq. (45), we employed the following dimensionless constitutive equation:

$$\tau_{rz} = \left\{\frac{Bn[1 - \exp(-M\dot{\gamma})]}{\dot{\gamma}} + 1\right\} \frac{\partial u_z}{\partial r}, \tag{50}$$

where

$$M \equiv \frac{mV}{R} \tag{51}$$

and $m$ is the Papanastasiou regularization parameter.

For the spatial discretization of the problem (44) and (50) with the conditions (8), we used the finite element method with quadratic ($P^2$-$C^0$) elements for the velocity. For the time discretization, we used the standard fully-implicit (Euler backward-difference) scheme. At each time step, the nonlinear system of discretized equations was solved by using the Newton method with a convergence tolerance equal to $10^{-5}$.

The results presented in this work have been obtained with 100 elements. Our numerical experiments with meshes of different refinement (ranging from 25 up to 400 elements) showed that the solutions obtained with the aforementioned optimal meshes are convergent. In particular, the calculated velocity profiles in the case of steady-state Bingham flow agreed well with the steady-state solutions shown in Fig. 6. The effect of the time step has also been studied. As in [3], the time step should be reduced as the Bingham number or the regularization parameter $M$ is increased, in order not only to ensure satisfactory accuracy but, more importantly, to ensure the convergence of the Newton–Raphson process which becomes very slow. In general, for $M = 300$, the time step ranged from $10^{-4}$ ($Bn = 0$) to $10^{-6}$ ($Bn = 20$); these values were further reduced by the code whenever the Newton–Raphson process failed to converge.

The code has also been tested by solving first the Newtonian flows and making comparisons with the analytical solutions. The agreement between the theory and the calculations was excellent. In particular, for all values of $\kappa$ in Fig. 3, the calculated volumetric flow rates coincided with the theoretical ones. The latter were calculated using MAPLE [12] and taking into account the leading 100 terms of the series in Eq. (15). In this section, we have chosen to present results only for $\kappa = 0.5$ and 0.1 with the imposed pressure gradient $f$ set equal to zero. The effect of the dimensionless growth parameter $M$ has also been studied, leading to similar conclusions as in [3]. In the results presented here, $M = 300$.

Fig. 7 shows the evolution of the velocity for a Newtonian ($Bn = 0$) and a Bingham ($Bn = 20$) fluid, with $\kappa = 0.5$. The numerical solution in Fig. 7a compares very well with the analytical solution, Eq. (13), for the Newtonian flow. The numerical solution for the Bingham flow (Fig. 7b) confirms that cessation is accelerated as the Bingham number is increased. Fig. 8 presents the evolution of the volumetric flow rate for various Bingham

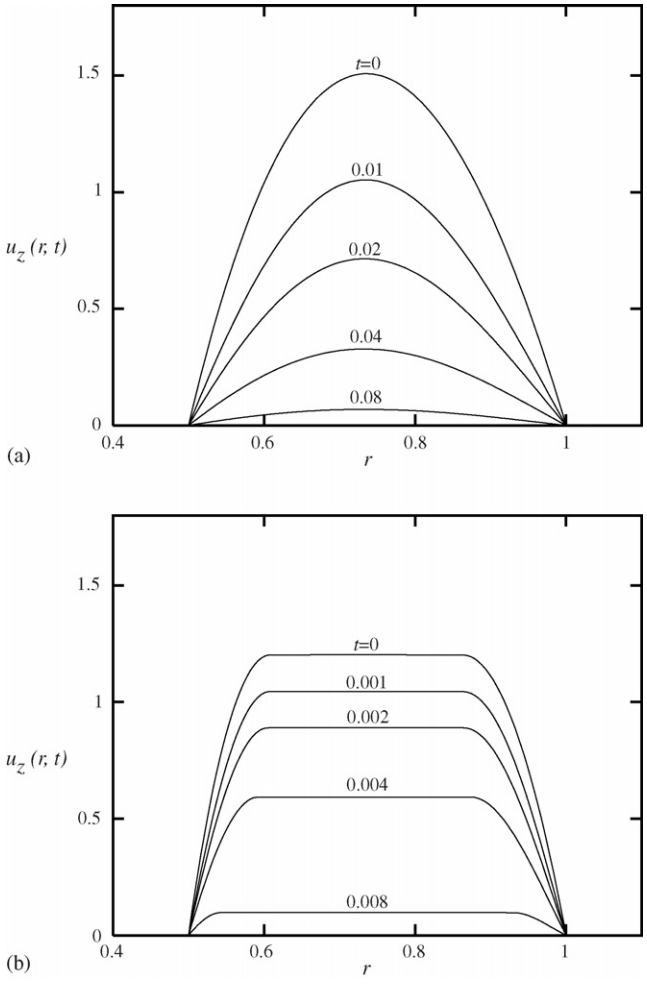


Fig. 7. Evolution of the velocity in cessation of annular Poiseuille flow with $\kappa = 0.5$: (a) Newtonian fluid; (b) Bingham fluid with $Bn = 20$.

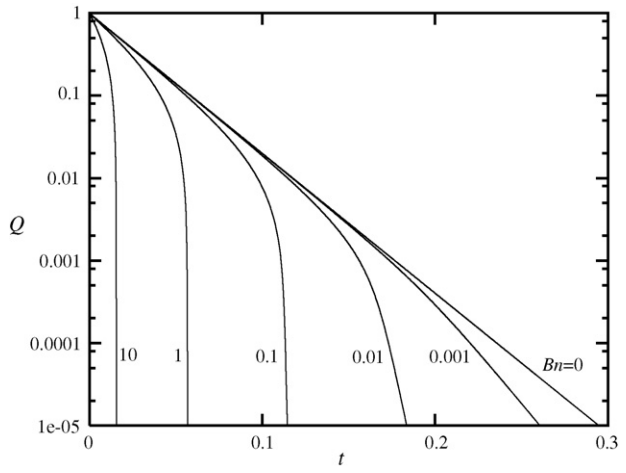


Fig. 8. Evolution of the volumetric flow rate in cessation of annular Poiseuille flow for various values of the Bingham number and $\kappa = 0.5$.

numbers. These curves demonstrate the dramatic effect of the yield stress, which accelerates the cessation of the flow.

The results obtained for other values of the diameter ratio, $\kappa$, are quite similar. Fig. 9 shows the evolution of the velocity

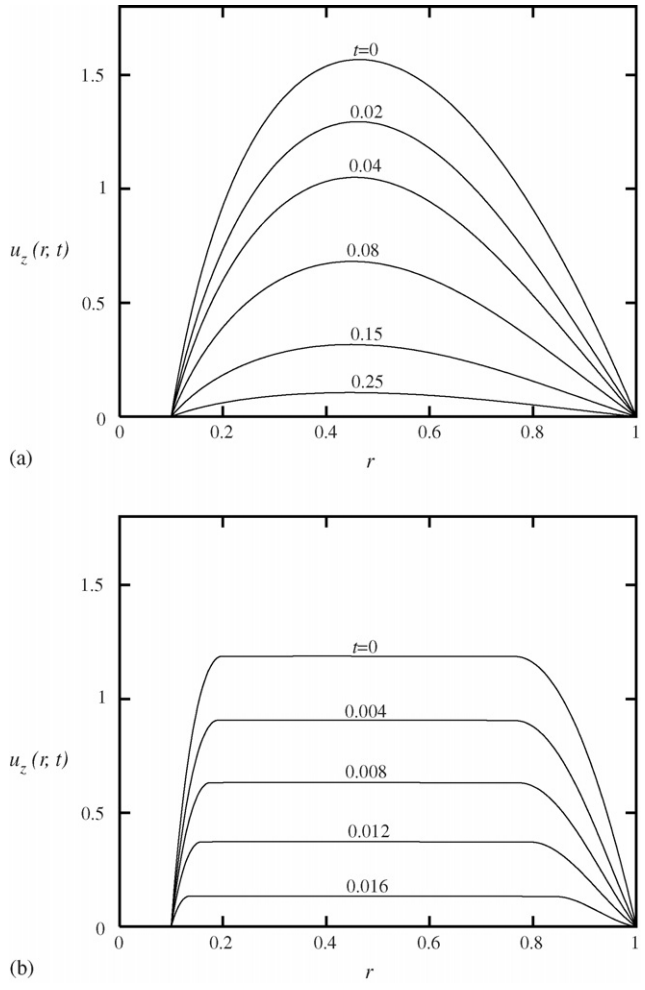


Fig. 9. Evolution of the velocity in cessation of annular Poiseuille flow with $\kappa = 0.1$: (a) Newtonian fluid; (b) Bingham fluid with $Bn = 20$.

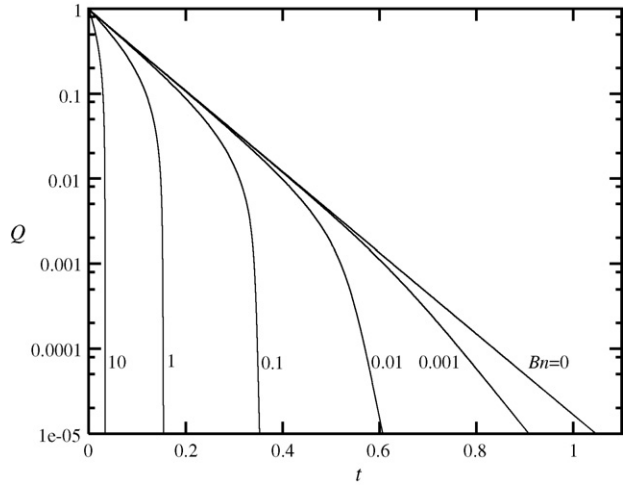


Fig. 10. Evolution of the volumetric flow rate in cessation of annular Poiseuille flow for various values of the Bingham number and $\kappa = 0.1$.

for $\kappa = 0.1$ and $Bn = 0$ and 20. The evolution of the volumetric flow rate for $\kappa = 0.1$ and various values of the Bingham number is shown in Fig. 10. It should be noted that the stopping times increase as the diameter ratio is reduced.

In order to make comparisons with the theoretical upper bound (49), we consider the numerical stopping time, $T_f$, as the time at which $Q = 10^{-5}$ is reached. As pointed out in our previous work [3], using a lower value of $Q$ does not affect the numerical stopping time for moderate and high Bingham numbers ($Bn > 0.1$). For low Bingham numbers ($Bn < 0.1$), however, the stopping time increases (see Figs. 14 and 15 in [3]). In Fig. 11, we compare the numerical stopping times for $\kappa = 0.1$ and 0.5 with the theoretical upper bounds. For moderate and high Bingham numbers, the computed stopping times are just below the theoretical upper bound given in Eq. (49). As discussed in [3], the small discrepancies observed for small values of the Bingham number are due to the fact that the value of the regularization parameter $M$ is not sufficiently high. For very small $Bn$, the effect of $M$ is not crucial, since the material is prac-

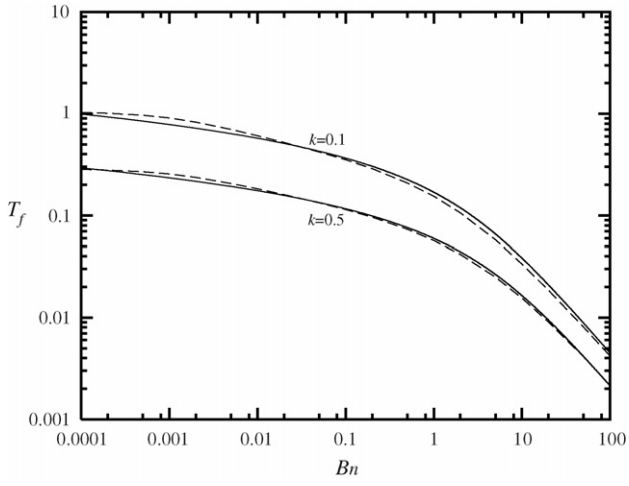


Fig. 11. Comparison of the numerical stopping times (dashed lines) with the theoretical upper bounds (solid lines) for $\kappa = 0.1$ and 0.5.

tically Newtonian, which explains why the numerical stopping time falls again below the theoretical upper bound.

## 5. Conclusions

The Papanastasiou modification of the Bingham model has been employed in order to solve numerically the cessation of the annular Poiseuille flow of a Bingham plastic. Unlike their counterparts in a Newtonian fluid, the stopping times for complete cessation are finite, in agreement with theory. The numerical stopping times are found to be in very good agreement with the theoretical upper bound provided by Glowinski [6], for moderate and high Bingham numbers. Some minor discrepancies observed for rather low Bingham numbers can be reduced by increasing the regularization parameter introduced by the Papanastasiou model. These results can be helpful in establishing stopping times in drilling exploration for drilling muds, where annular geometries are encountered.

## Acknowledgements

Part of this research is supported by the "HERAKLEITOS" program of the Ministry of Education and Religious Affairs of Greece (#68/0655). The Project is co-funded by the European Social Fund (75%) and National Resources (25%). This research was also partially supported by the Research Committee of the University of Cyprus. Financial support from the program "SOCRATES" for scientific exchanges between Greece and Cyprus is gratefully acknowledged.

## References

[1] N.J. Balmforth, I.A. Frigaard, Introduction: visco-plastic fluids, from theory to application, J. Non-Newtonian Fluid Mech., submitted for publication (Special Issue).
[2] P. Coussot, Rheometry of Pastes, Suspensions, and Granular Materials: Applications in Industry and Environment, Wiley, New York, 2005.
[3] M. Chatzimina, G. Georgiou, I. Argyropaidas, E. Mitsoulis, R.R. Huilgol, Cessation of couette and poiseuille flows of a bingham plastic and finite stopping times, J. Non-Newtonian Fluid Mech. 129 (2005) 117.
[4] T.C. Papanastasiou, Flows of materials with yield, J. Rheol. 31 (1987) 385.
[5] I.A. Frigaard, C. Nouar, On the usage of viscosity regularization methods for visco-plastic fluid flow computation, J. Non-Newtonian Fluid Mech. 127 (2005) 1.
[6] R. Glowinski, Numerical Methods for Nonlinear Variational Problems, Springer-Verlag, New York, 1984.
[7] R.R. Huilgol, B. Mena, J.M. Piau, Finite stopping time problems and rheometry of Bing-ham fluids, J. Non-Newtonian Fluid Mech. 102 (2002) 97.
[8] T. Papanastasiou, G. Georgiou, A. Alexandrou, Viscous Fluid Flow, CRC Press, Boca Raton, 1999.
[9] C.-S. Yih, Fluid Mechanics, West River Press, Ann Arbor, 1979.
[10] R.B. Bird, G.C. Dai, B.J. Yarusso, The rheology and flow of viscoplastic materials, Rev. Chem. Eng. 1 (1982) 1.
[11] P. Szabo, O. Hassager, Flow of viscoplastic fluids in eccentric annular geometries, J. Non-Newtonian Fluid Mech. 45 (1992) 149.
[12] MAPLE 9, Advanced Programming Guide, MapleSoft, Waterloo MAPLE Inc., 2003.